Supporting Information

Atomic Layers of Graphene for Microbial Corrosion Prevention

Govind Chilkoor^{†§}, Namita Shrestha[‡], Alex Kutana[∇], Manoj Tripathi⁺, Francisco C Robles Hernández[∥], Boris I. Yakobson[∇], Meyya Meyyappan[⊥], Alan B. Dalton⁺, Pulickel M. Ajayan[∇]*, Muhammad M. Rahman[∇]*, Venkataramana Gadhamshetty†§*

†Department Civil and Environmental Engineering, South Dakota School of Mines and Technology, Rapid City, SD 57701, USA

§2Dimensional Materials for Biofilm Engineering Science and Technology (2DBEST) Center, South Dakota School of Mines and Technology, Rapid City, SD 57701, USA

‡Department of Civil and Environmental Engineering, Rose-Hulman Institute of Technology, Terre Haute, IN 47803, USA

∇Department of Materials Science and NanoEngineering, Rice University, TX 77005, USA ⁺Department of Physics and Astronomy, University of Sussex, Brighton BN1 9RH, U.K. ^{||}Department of Mechanical Engineering Technology, University of Houston, TX 770204, USA

¹Center for Nanotechnology, NASA Ames Research Center, Moffett Field, CA 94035, USA

Contents

Optical, SEM, TEM, Raman, and contact angle analysis of SLG- Cu and MLG-Cu	2
Preparation of Sulfate-reducing bacterial (SRB) strain and its culture	2
Microbial corrosion experiments	3
Electrochemical measurements	3
Characterization of biofilm and corrosion deposits	4
EEC circuit	5
Density functional theory (DFT) calculations	5
Results and discussion	7
Additional Figures	11

Optical, SEM, TEM, Raman, and contact angle analysis of SLG- Cu and MLG-Cu

To analyze the graphene samples by optical and Raman spectroscopy, we transferred the films to a SiO₂/Si substrate using the PMMA procedure detailed in previous literature. The optical images were obtained using a Carl Zeiss Axio vision microscope in bright field mode using a 10X HD-DIC objective lens. The images were captured using a Zeiss Axio Cam MRC 5 camera and later processed using Axiovision SE64 software. A Zeiss Supra40 scanning electron microscope (SEM) equipped with X-ray microanalysis was used to get the images of the graphene films on copper foil. For TEM analysis, the films were transferred onto a Holey carbon support film on a Cu 400 mesh grid. JEM-2100 LaB6 Transmission Electron Microscope (TEM) (JEOL, USA) was used to obtain high-resolution TEM (HRTEM) images and selected area electron diffraction (SAED) patterns. Raman spectrometer equipped with a microscope (Foster + Freeman Ltd, Evesham, UK) was used to obtain the peaks for SLG and MLG films transferred on to a SiO₂/Si wafer. The measurements were carried at an incident power of 10 mW, a laser excitation wavelength of 532 nm, and using a 100-objective lens. The wettability of the graphene coatings was evaluated by a contact angle goniometer (Model 500, ramé-hart Instrument Co.). The obtained water droplets were analyzed by DROP-image Advanced v 2.4 software to estimate the water contact angle (WCA).

Preparation of Sulfate-reducing bacterial (SRB) strain and its culture

The *Desulfovibrio alaskensis* strain G20 (DA-G20) was anaerobically grown in the Lactate C (L-C) medium containing the following constituents (g/L): sodium lactate, 6.8; sodium sulfate, 4.5; sodium citrate, 0.3; dehydrated calcium chloride, 0.06; ammonium chloride, 1.0; magnesium sulfate, 2.0; potassium phosphate monobasic, 0.5 and yeast extract, 1.0.² The listed L-C medium components were mixed thoroughly using type III ASTM Standards for Laboratory Reagent Water

(ASTM D1193-91). The pH of the medium was adjusted to 7.2 and then sterilized by autoclaving at 121 $^{\circ}$ C for 30 min. The DA-G20 cultures were grown in 150 mL serum bottles containing 100 mL of L-C having a headspace of N₂-H₂ (95% N2 v/v and 5% H₂ v/v). DA-G20 cultures were incubated at 30 $^{\circ}$ C using modest agitation (125 rpm) on an orbital platform shaker for 48 h.

Microbial corrosion experiments

MIC experiments were carried out in a 400 mL single compartment corrosion Cell (Gamry Instruments) consisting of a graphite plate as a counter electrode, an Ag/AgCl as a reference electrode (RE), and the sample of interest as a working electrode (WE). The graphene-coated copper samples were mounted laterally on a stainless-steel sample bracket (Gamry part # 990-00254) facing the L-C growth medium. An electroplating tape was used to limit the exposure area to 1 cm² of coated copper samples. Before inoculating with DA-G20, the corrosion cell having the L-C growth medium was purged with sterile nitrogen gas (15 psi) for 30 min to obtain an anaerobic condition. The MIC experiments were performed at 30 °C and with an initial inoculum of 10% (v/v), a pH of 7.2, and a cell count = 10^5 cells/mL.

Electrochemical measurements

Linear polarization resistance (LPR) tests were run in triplicate using the following parameters: potential = ± 10 mV (vs. open-circuit potential (OCP)), scan rate = 0.125 mV/s, initial delay = 1200 s, and stability = 0.1 mV/s. Corrosion rates from the LPR tests were determined using the Tafel constant values for the anodic and cathodic slopes from the Tafel experiment. The cyclic voltammetry (CV) tests were carried out consecutively for four different cycles under a potential range of -700 mV to +500 mV (vs. Ag/AgCl) and a scan rate of 0.1 mV/s. The Potentiodynamic polarization (PDP) tests were carried out in the potential range of - 300 mV to 1000 mV (vs. OCP) with a scan rate of 0.2 mV/s. Electrochemical impedance spectroscopy (EIS)

tests were performed at the OCP using an AC signal with an amplitude of ± 10 mV, and the corresponding EIS spectra were obtained in the 10000 to 0.01 Hz range. Gamry Echem Analyst was used to fit the EIS results to an electrical equivalent circuit (EEC).

Corrosion rates (mils per year (mpy)) were determined by substituting R_p and I_{corr} values obtained from equation (1) in equation (2).

$$i_{corr} = \frac{\beta_a \beta_c}{(\beta_a + \beta_c)} \times \frac{1}{2.3 R_p} = \frac{B}{R_p}$$
 (1)

where β_a and β_c are the anodic and cathodic Tafel constants, respectively, R_p is the polarization resistance, and B is the Stern-Geary coefficient. The Tafel constants were obtained from Tafel analysis that was carried out with a scan rate of 1 mV/s.in the potential range of \pm 250 mV (vs. OCP).

Corrosion rate
$$(mpy) = \frac{K i_{corr}(E.W)}{\rho A}$$
 (2)

where the constant $K = 1.288 \times 10^5$ milli-inches as used to obtain corrosion rates in mpy. E.W, ρ , and A are the equivalent weight (31.7 g), density (8.94 g/cm³), and area (1 cm²) of the Cu specimen, respectively. The protection efficiency was calculated by substituting the values of current density obtained from Tafel analysis in the equation.

Characterization of biofilm and corrosion deposits

A Zeiss Supra40 variable pressure field emission SEM fitted with an advanced system for X-ray microanalysis (Oxford Aztec Energy) was used to obtain the surface morphology and elemental composition of the biofilm and the corrosion products. The SEM was operated using an accelerated voltage of 5 kV for imaging and 15 kV to determine the elemental composition of the corrosion products.

EEC circuit

The EEC circuit includes a solution resistance (R_s) in series with single time constants one representing the metal/ electrolyte interface for Faradaic charge transfer resistance (R_{ct}) and the capacitance due to the double layer (Q_{dl}) (**Figure S3a**). The value of the constant phase element capacitance (Q) was converted into capacitance (Q) by using its corresponding resistance (Q) value using equation (3).

$$C = R^{\left(\frac{1-n}{n}\right)} Q^{\frac{1}{n}} \tag{3}$$

where n is the exponent in the constant phase element

Density functional theory (DFT) calculations

Work functions were calculated from density functional theory using local density approximation (LDA) functional, as implemented in the Quantum Espresso.⁴ Scalar relativistic ultrasoft pseudopotentials were used to represent ionic cores, as implemented in the pslibrary,⁵ and 50 Ry kinetic energy cutoff was used. A k-grid of 21×21×1 was used for Brillouin zone sampling, with Gaussian smearing. Cu(111) and Ni(111) surfaces were represented by 6-layer slabs, Bernal (AB) stacking was used for multi-layer graphene, and a vacuum space of 15 Å between the periodic images was added in the normal direction in all calculations. Dipole correction was used in the normal direction. The graphene-metal distance (d) was defined as the distance between the nearest graphene layer and a top layer of metal atoms, and the Z coordinate of the nearest graphene plane and the top metal layer was held fixed during geometry optimization. All other coordinates were relaxed using the Broyden–Fletcher–Goldfarb–Shanno (BFGS) algorithm until all unconstrained force components were less than 2.6 meV/Å. In calculating the work function, dipole correction

was applied in the direction normal to the surface, and the work function was defined as the difference between the vacuum potential outside of the graphene and Fermi level (**Figure S4**).

The Raman measurements were carried out with a 532 nm laser line, 1800 grating line/mm using the Renishaw inViaTM 100X optical lens. The laser power was limited to 5% (< 1mW) throughout the duration. The Raman peaks were fitted using the Lorentzian function to measure the peak positions for G and 2D peak. For evaluating the strain and doping characteristics of graphene using a correlation plot, the strain (ε) and the charge carrier concentration (n) of graphene were related to Raman shift (G, 2D) as presented in equation (4).

$$\binom{G}{2D} = T \binom{\varepsilon}{n} \tag{4}$$

where

$$T = \begin{pmatrix} -2\gamma_G G^0 & k_G \\ -2\gamma_{2D} 2D^0 & k_{2D} \end{pmatrix} \tag{5}$$

 γ is the Grüneisen parameter, k is the doping shift rate, and Go and 2Do are values of no-strain and no-doping peak position. In graphene, γ G =1.95, γ 2D = 3.15, k_G = -1.407 × 10⁻¹² cm^{-1} and k_{2D} = -0.285 × 10⁻¹² cm^{-1} .^{6, 7} It is worthy to note that (n) mostly considers the effects of coupling with the substrate, however local environmental conditions (e.g., relative humidity) and stimulating conditions (e.g. potential bias, corrodent, airborne impurities, ion doping) may further influence n and ε .

The Kelvin probe force microscopy (KPFM) investigation was performed using atomic force microscopy (AFM)-Bruker Dimension Icon. Peak-force KPFM through two pass modes has been used in the characterization; in the first pass, a topography image was collected, and the second pass for the potential map (contact potential difference, CPD). Conductive tip from Bruker

(Model: PFQNE-Al, stiffness $\approx 0.8\pm0.2$ N/m, diameter ≈ 5 nm, resonance frequency = 300 KHz) has been used for the measurements. The calculation of the tip work function (WF) was carried out using freshly cleaved HOPG using the relation, WF_{sample} = WF_{tip} – eVdc. The same relation was used to measure the local WF of the pristine and exposed samples.

Results and discussion

Protection ability of atomic graphene layers on Nickel (Ni) substrates: We further explored the protective ability of atomic graphene layers on nickel (Ni) substrates. First, we carried out density functional theory (DFT) simulations to study the WF behavior of Ni (111) modified with SLG and MLG, for graphene-Ni interlayer distance (d) ranging up to 6 Å. Next, KPFM was conducted to experimentally study the WF behavior of SLG-Ni and MLG-Ni substrates exposed to a corrosive environment (2 h, 1M H₂SO₄). Finally, we carried out Raman analyses to study the doping and strain behavior of the SLG-Ni in comparison to those of SLG-Cu, both exposed to the H₂SO₄ corrodent.

Upon adsorption of graphene layers, Ni (111) showed a significant drop in the WF values as a function of graphene-Ni interlayer distance (d) (**Figure S5**). At d < 3 Å, the WF of SLG-Ni (\sim 3.5 eV) and MLG-Ni (\sim 4.7 eV) was significantly lower than bare Ni (\sim 5.4 eV). The SLG-Ni and MLG-Ni displayed lower WF even for 3 Å<d <6 Å (**Figure S5**). Interestingly, SLG-Ni experienced the highest drop in the WF (Δ WF = -1.9 eV) compared to MLG-Ni (Δ WF = -0.7 eV) at d < 3 Å. Even, the WF of SLG-Ni (\sim 3.5 eV) is found to be lower than free-standing graphene (\sim 4.6 eV). The lower the WF the greater is the activity of the electrons that participate in relevant electrochemical processes, lower (more negative) is the corrosion potential and weaker is the protective ability of atomic graphene layers. Thus, MLG-Ni is expected to offer superior corrosion

protection compared to SLG-Ni, similarly aligned with the findings from the Cu test case (**Figure 4**).

Next, we conducted KPFM tests to assess experimentally the WF behavior of SLG-Ni and MLG-Ni exposed to 1M H₂SO₄, a corrodent typical to MIC conditions (**Figure S6**). An epitaxially grown SLG film on polycrystalline Ni substrates was used for the KPFM study. The report from the KPFM study corroborate the findings from DFT analysis: (1) WF of the both MLG-Ni (~4.95 eV) and SLG-Ni (~4.75 eV) are lower than Ni (~4.98 eV); (2) Upon exposure to the corrodent, WF of both SLG-Ni and MLG-Ni experienced a significant drop in WF. The ΔWF for SLG-Ni (~200 meV) and MLG-Ni (~50 meV) was two-fold and four-fold lower than bare Ni, respectively. However, ΔWF for MLG-Ni was four-fold lower than SLG-Ni, corroborating that MLG offers better corrosion protection to Ni.

Convoluted strain and doping effect behavior of graphene layers exposed to 1M H₂SO₄: Our Raman studies confirmed that the atomic graphene layers on both Cu and Ni substrates stayed intact even after the prolonged exposure to the 1M H₂SO₄ corrodent (Figure S7a, S7b). However, upon the exposure, both SLG-Cu and SLG-Ni displayed a convoluted strain and doping effect, shown by the systematic shift in G and 2D peaks, respectively (Figure S7). We report that SLG-Ni displays a distinct doping behavior compared to SLG-Cu, as shown in the correlation plot (Figure S7c). While SLG-Ni experienced a compressive strain with minimal change in the carrier concentration (n), SLG-Cu experienced a notable increase in the carrier concentration (n) with an incremental change to the tensile strain. These results suggest that SLG-Cu is more prone to corrosion compared to SLG-Ni, aligning with the results of the DFT simulations. For example, Ni (111) experienced a decrease in WF only when modified with SLG

(Figure S5); whereas, Cu (111) experienced a decrease in WF when modified with SLG as well as with MLG (2 and 3 layers, respectively) (Figure 4).

The pristine SLG-Ni and SLG-Cu samples also displayed a varying degree of the deconvoluted strain and doping effect. The differences can be attributed to the differences in the nature of the coupling between atomic graphene layers with their respective substrates. The pristine forms of SLG-Ni and SLG-Cu lie at a different location of the doping axis (brown line), suggesting a varying extent of doping of the two substrates. The distribution of Raman data for pristine SLG-Cu illustrates the lower carrier concentration as compared to SLG-Ni. This variation is attributed to the differences in the metallic characteristics of the two substrates, resulting in a different electron-phonon coupling. The SLG-Ni exposed to the corrodent displayed a higher compressive strain with minimal change in doping concentration compared to the pristine SLG-Ni (shaded by yellow color). However, upon the exposure, the SLG-Cu experienced a significant increase in the tensile strain as well as carrier concentration (fewer negative values of n as shaded by green color) compared to the pristine region. A considerable distribution of peaks of graphene over Cu is due to a change in the physical texture of the Cu surface after exposure to the corrodent, which was mitigated over Ni. This finding indicates that SLG-Cu is more vulnerable to 1M H₂SO₄ corrodent compared to SLG Ni, agreeing with the findings of the KPFM studies.

Effects of surface roughness on corrosion behavior. We discuss the effect of the different copper surfaces as shown in Figure 2 on the corrosion behavior. The water contact angle values (Figure 1h-j) or the wetting characteristics of bare Cu surface are related to its higher roughness due to highly oxidized surfaces especially at the striation's steps produced during foil's processing (Figure 2b). These oxidized steps at striation are active sites (*i.e.* with more ledges and kinks) to interact with corrodents. Such surface corrugation fluctuates the electron work function which is

predicted to promote corrosion.⁸ It has been reported that electrons in the vicinity of the peak of a protrusion are easier to escape than those in trough sites, thus peak region would be a preferential corrosion site.⁹ The annealing of the Cu surface in the CVD chamber minimizes the striation and flatten the surface. Subsequently, the epitaxially grown graphene over Cu surface induces hydrophobic characteristics with an elevation of nearly 10 degrees in contact angle.

Additional Figures

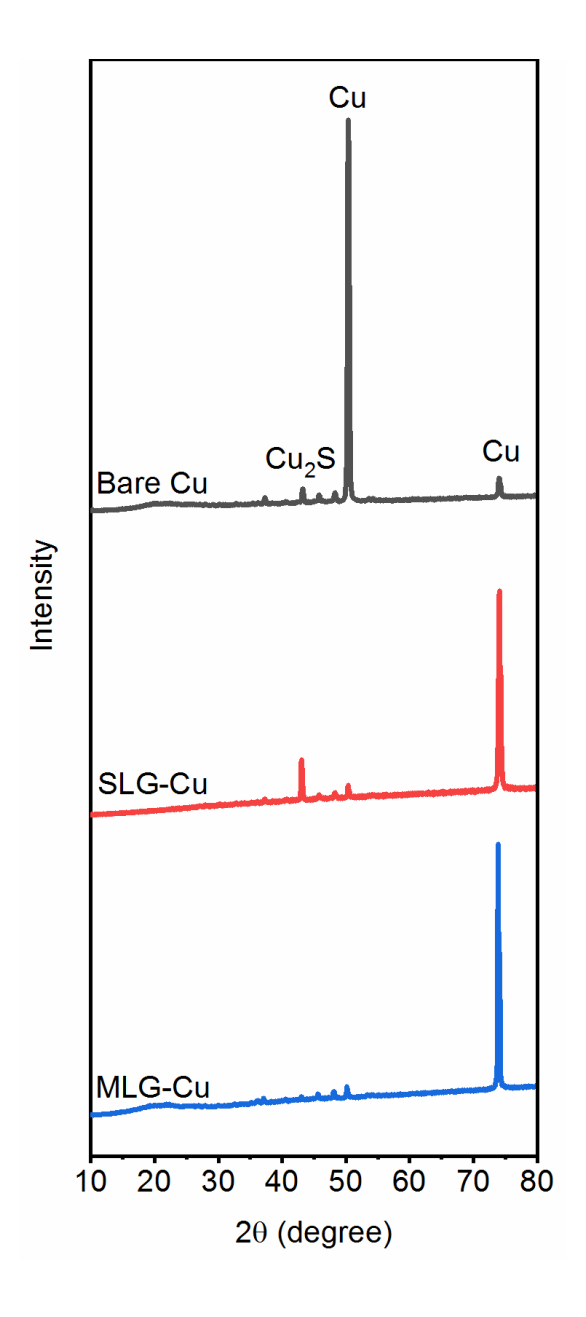


Figure S1. XRD data shows prominent peaks of chalcolite (Cu₂S) for bare Cu and SLG-Cu compared to MLG-Cu.

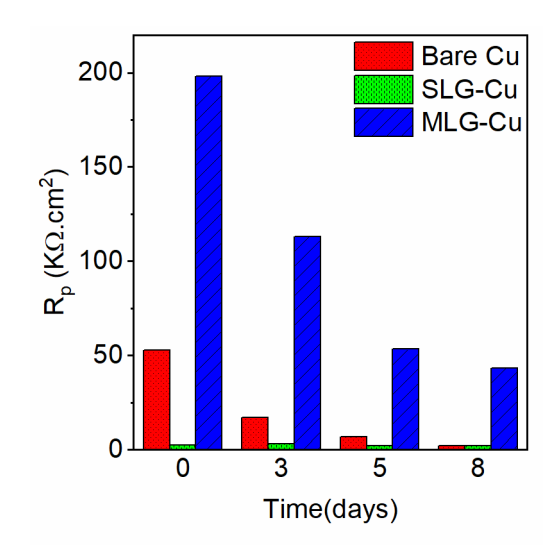


Figure S2. Polarization resistance (R_p) values for bare Cu, SLG-Cu, and MLG-Cu obtained from linear polarization test

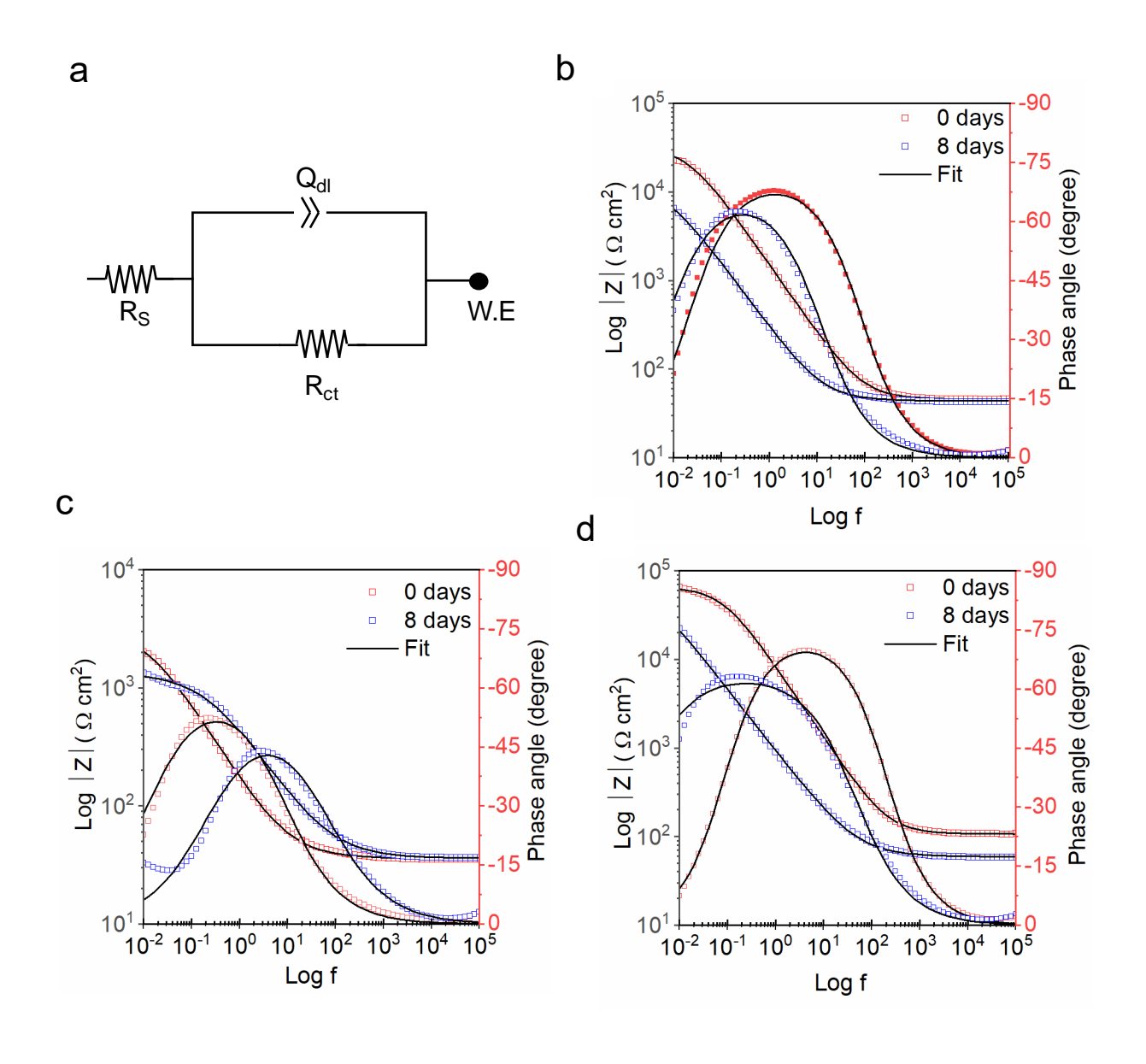


Figure S3. (a) Electrical equivalent circuit used to fit Bode magnitude data for (b) bare Cu (c) SLG-Cu and (d) MLG-Cu on day 0 and 8. The EEC models fit are in solid black lines.

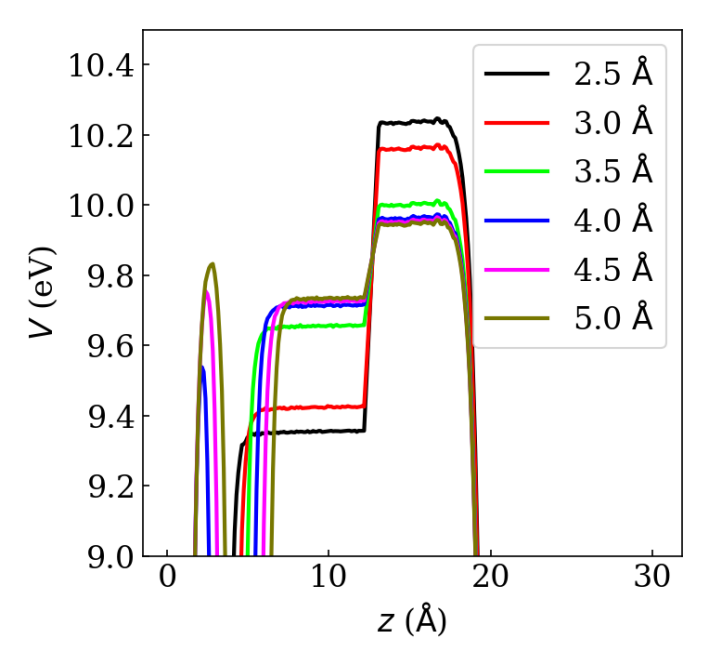


Figure S4: Calculated electrostatic potential at different monolayer graphene-Cu separations with dipole correction applied. The size of the supercell in the *z*-direction is 30.4 Å, with the vacuum region being in the middle of the figure, at *z* between \sim 8 and 17 Å.

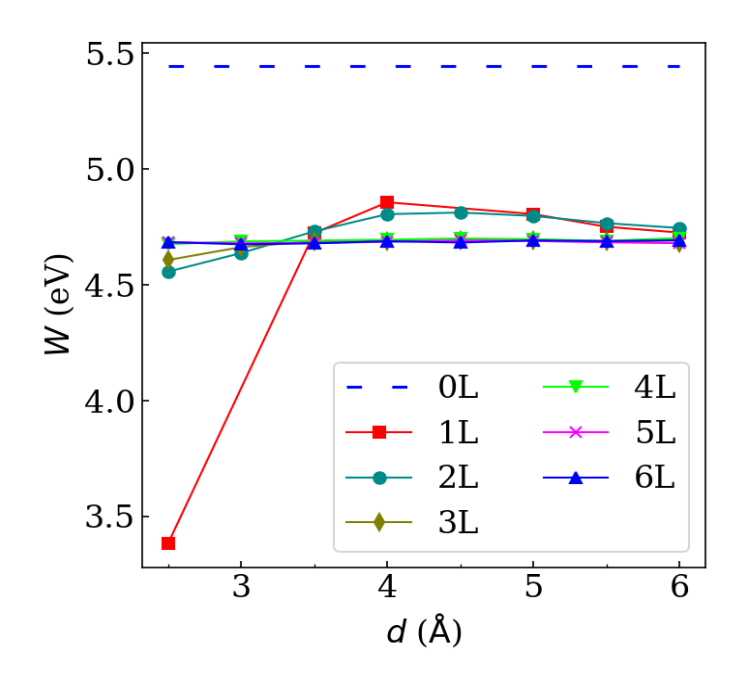


Figure S5. Work function (WF) of Ni (111) adsorbed with 1 to 6 layers of graphene as a function of the graphene-Ni interlayer distance (d). Symbols show calculated WF values for SLG-Ni, MLG-Ni, and dashed blue line of Ni (111).

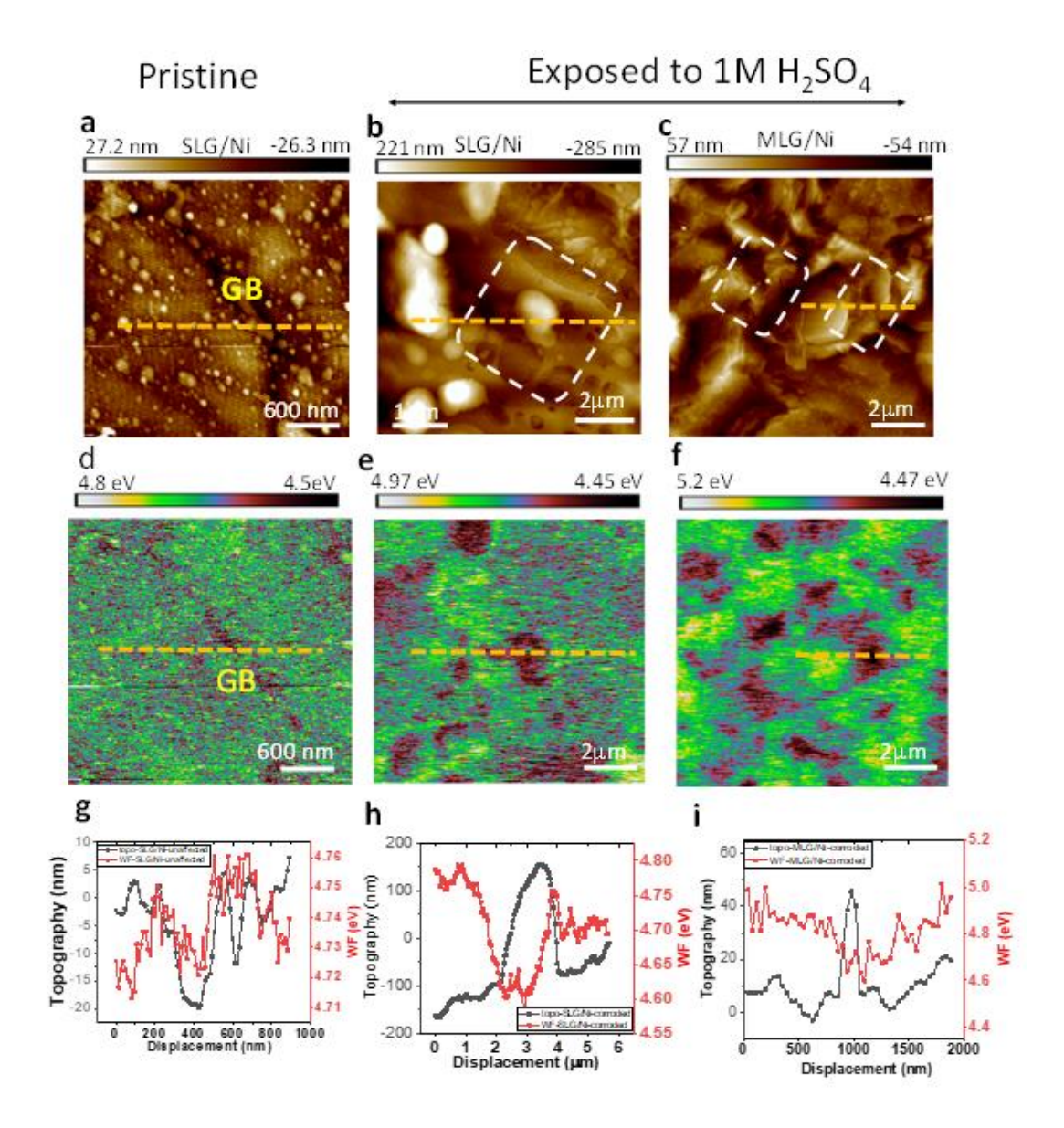


Figure S6. Morphology and surface potential map of the graphene layers covered Ni substrates. (a-c) topography of pristine SLG-Ni, exposed SLG-Ni and MLG-Ni substrates. The white dashed rectangle represents the salts resulting from exposure to 1M sulfuric acid corrodent. (d-f) show the corresponding WF map (obtained from the surface potential) for the three samples. The dark regions in (d) depict the grain boundaries characterized by lower WF, both in the pristine and exposed regions. (g-i) shows the superimposed topographic profiles and WF map to illustrate the WF of grain and GB in the three samples. Orange dashed lines in (d-f) indicate the location of the local topography and its corresponding surface potential values that were converted into WF (eV).

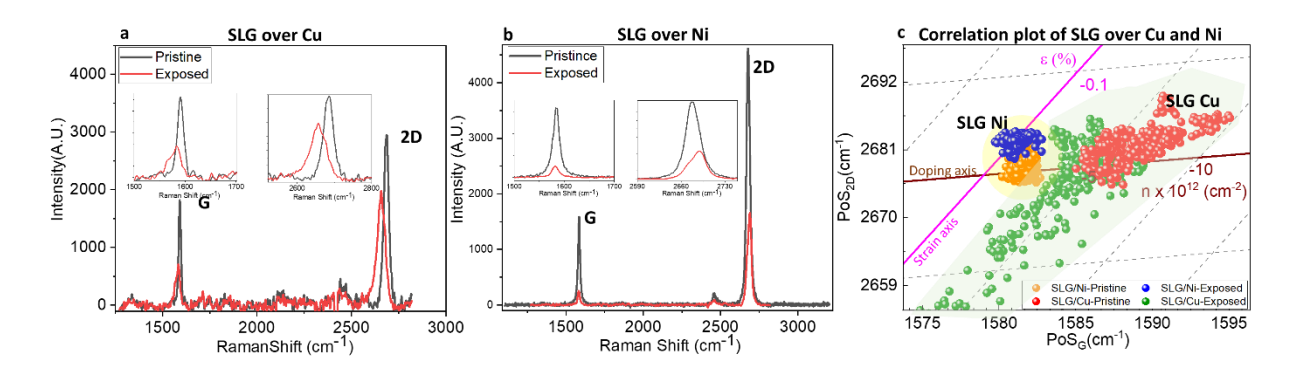


Figure S7. Deconvolution and doping behavior of SLG-Cu and SLG-Ni exposed to the 1M H₂SO₄ corrodent. (a) Raman spectra of pristine SLG over Cu at the pre and post-exposure. The G and 2D peak of the graphene shows redshift in the Raman modes in SLG over Cu at the exposed region. Inset shows the resolved peak shifting of G and 2D peak. (b) The Raman spectra of SLG over Ni shows a blue shift in the corroded region, which is resolved in the inset. (c) Correlation plot of ~500 spectra for SLG over Cu and Ni at the pre- and post-exposure conditions. The pink and brown lines represent strain (ε) and doping (n) axis, respectively; the intersection region is considered as minimal doping and strain regions. The deviation from the intersection coordinates is evaluated as an effect of corrodent on graphene over the two different metals.

References

- (1) Chilkoor, G.; Karanam, S. P.; Star, S.; Shrestha, N.; Sani, R. K.; Upadhyayula, V. K.; Ghoshal, D.; Koratkar, N. A.; Meyyappan, M.; Gadhamshetty, V., Hexagonal Boron Nitride: The Thinnest Insulating Barrier to Microbial Corrosion. *ACS Nano* **2018**, *12*, 2242-2252.
- (2) Sani, R. K.; Geesey, G.; Peyton, B. M. Assessment of Lead Toxicity to *Desulfovibrio Desulfuricans* G20: Influence of Components of Lactate C Medium. *Adv. Environ. Res.* **2001,** *5*, 269-276.
- (3) Hirschorn, B.; Orazem, M. E.; Tribollet, B.; Vivier, V.; Frateur, I.; Musiani, M., Determination of Effective Capacitance and Film Thickness from Constant-Phase-Element Parameters. *Electrochim. Acta* **2010**, *55*, 6218-6227.
- (4) Giannozzi, P.; Andreussi, O.; Brumme, T.; Bunau, O.; Nardelli, M. B.; Calandra, M.; Car, R.; Cavazzoni, C.; Ceresoli, D.; Cococcioni, M. Advanced Capabilities for Materials Modelling with Quantum ESPRESSO. *J. Phys.: Condens. Matter* **2017**, *29*, 465901.
- (5) Dal Corso, A., Pseudopotentials Periodic Table: From H to Pu. *Comput. Mater. Sci.* **2014**, *95*, 337-350.
- (6) Lee, J. E.; Ahn, G.; Shim, J.; Lee, Y. S.; Ryu, S., Optical Separation of Mechanical Strain from Charge Doping in Graphene. *Nat. Commun.* **2012**, *3*, 1-8.
- (7) Jiang, T.; Wang, Z.; Ruan, X.; Zhu, Y., Equi-Biaxial Compressive Strain in Graphene: Grüneisen Parameter and Buckling Ridges. *2D Mater.* **2018**, *6*, 015026.
- (8) Li, W.; Li, D. Y. Influence of Surface Morphology on Corrosion and Electronic Behavior. *Acta Mater.* **2006**, *54* (2), 445–452.
- (9) Hu, M.; Zhang, W.; Shang, X.; Wen, J.; Zhao, Z.; Qiao, B.; Kong, D.; Dong, C. Effect of Surface Roughness on Copper Corrosion in Simulated Beishan Groundwater, China. *Int. J. Electrochem. Sci.*, **2020**, *15*, 2961-2972